JOURNAL OF GUIDANCE, CONTROL, AND DYNAMICS
Vol. 48, No. 4, April 2025

Technical Notes

Line-of-Sight-Constrained Multicopter Interceptability

Kun Yang,* Chenggang Bai,† and Quan Quan‡
Beihang University, 100191 Beijing, People's Republic of China

https://doi.org/10.2514/1.G008527

Downloaded by BEIHANG UNIVERSITY on March 30, 2025 | http://arc.aiaa.org | DOI: 10.2514/1.G008527

I. Introduction

IN RECENT years, the application of multicopter unmanned aerial vehicles (UAVs) has experienced rapid growth across diverse sectors, including surveillance, reconnaissance, delivery, and entertainment [1–4]. Alongside their widespread use, there has been an increasing recognition of the security risks associated with unauthorized or hostile uses of multicopters. This has underscored the pressing necessity for developing effective countermeasures [5,6]. Consequently, the strategy of multicopter interception has become critically important in the context of aerospace defense [7,8].

Central to the interception process is the interceptor's ability to detect the target through its sensors and maintain the line of sight (LOS) within its field of view (FOV), a requirement known as the LOS constraint. This study explores the problem of target interception under the LOS constraint for multicopter interceptors. We employ a strapdown monocular camera as the primary sensor for the interceptor multicopters, drawing upon prior research that demonstrates the efficacy of monocular cameras in aerial interception tasks [9,10]. The use of monocular cameras allows for a more compact and streamlined interceptor design, thereby improving agility and precision.

Autonomous multicopter interception can be primarily divided into two categories: location-estimation-based methods and image-based visual servoing (IBVS)-based methods. In the Mohamed Bin Zayed International Robotics Challenge (MBZIRC) 2020 challenge, location-estimation-based methods were prominently utilized. These methods employ a comprehensive perception-planning-control framework to intercept both static and dynamic targets [11–13]. The success of these methods depends heavily on the accuracy of estimation, the rationality of planning, and the precision of control. In contrast, IBVS-based methods eliminate the planning module to reduce errors stemming from inaccurate location estimation and planning. These methods focus on bearing measurements, leading to innovations such as guidance laws [14,15] and the use of virtual cameras for tracking targets [16,17]. Our previous work has contributed to this field by developing an IBVS algorithm, which was tested using a strapdown monocular camera in real flight experiments [9,10].

Despite extensive research into various interception techniques, fundamental questions remain inadequately addressed: Is there a guidance law or controller that ensures that a given interceptor can complete the interception task? Furthermore, which type of interceptor is more effective for such tasks? This study aims to address these gaps by identifying the optimal interceptor configuration through reachability analysis, which involves defining a systematic measure for interception tasks.

Figure 1 illustrates two interception scenarios. The LOS is an imaginary line between the interceptor and the target. The unit vector along this line from the interceptor to the target is referred to as the *LOS vector*. In Fig. 1a, the multicopter successfully intercepts and maintains the target within its FOV, despite the target's maneuvering force $\boldsymbol{f}_{\text{unc}}$. The interceptor's strategy $\boldsymbol{f}_d$ aligns the net force $\boldsymbol{f}_{\text{net}}$ with the LOS vector, thereby closing the distance to the target. Conversely, Fig. 1b depicts a scenario where improper sensor setup prevents the alignment of the net force $\boldsymbol{f}_{\text{net}}$ with the LOS vector, resulting in increasing distance and interception failure. This scenario is common in practical applications, such as multicopters hovering at high altitudes to search for low-altitude intruders [1,2]. It is argued that such configurations are not ideally suited for interception missions. The objective is to theoretically determine optimal interceptor configurations for interception tasks by introducing a quantifiable measure of interceptability and employing it to optimize interceptor design. A detailed analysis is provided in Sec. III.

Interceptability under LOS constraints is studied, akin to a reachability problem where the goal is to reach a given state in finite time. The reachable set used in multicopter pursuit–evasion games [18–20] can be adapted to model the interception problem. Additionally, reachability analysis has been applied in parameter configuration design for both multicopters [21–23] and missiles [24–26]. However, current research does not consider LOS constraints and lacks analytical reachability criteria for nonlinear systems, typically relying on numerical computation. Building on recent work that presents a linear quadratic guidance law for joint motion planning of a pursuer–turret assembly considering LOS constraints [27], this Note proposes a new form of minimax optimization [28] for interception, accounting for the target's optimal strategy, and offers analytical calculation methods and configuration guidance for interceptors.

The contributions of this Note are as follows:

1) The global LOS-constrained interceptability is defined to theoretically determine whether a given interceptor can complete the interception task. This provides the theoretical basis for designing interceptor configurations, which are further used in guidance and control laws.

2) By integrating game theory and control theory, we propose a computational method for the degree of interceptability (DOI). The DOI serves as a global LOS-constrained interceptability criterion, allowing the measurement of an interceptor's ability to perform interception tasks.

3) Based on the DOI, we establish analytical criteria for the DOI of multicopters. Additionally, we provide recommendations for interceptor configuration design and verify their effectiveness through simulations and real flight experiments.

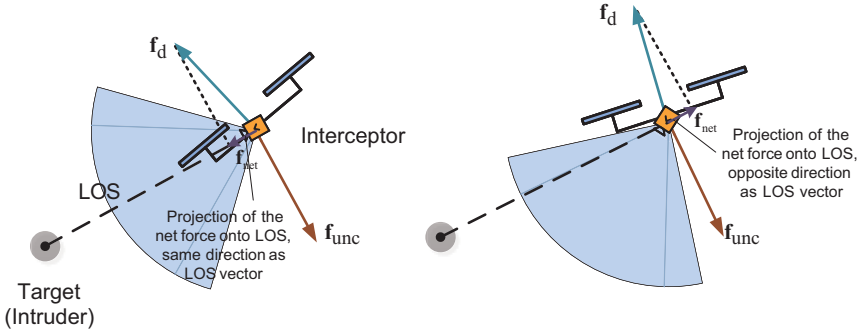
The remainder of this Note is organized as follows: In Sec. II, we establish the flight control rigid-body model of the interceptor relative to the target, define global LOS-constrained interceptability, and formulate the feasibility problem. In Sec. III, to solve the feasibility problem, we define the DOI and show that the system is interceptable if and only if the DOI is positive. We derive DOI calculation methods for multicopters and obtain interceptor configuration design guidelines based on the results. Finally, in Secs. IV and V, we use numerical simulations and real flight experiments to verify the optimality of the strategy, as well as the interception process and error for both interceptable and uninterceptable cases. The details of the simulations and experiments can be found at https://youtu.be/bz52TcHFS6A.

Received 29 May 2024; accepted for publication 2 October 2024; published online 13 December 2024. Copyright © 2024 by the American Institute of Aeronautics and Astronautics, Inc. All rights reserved. All requests for copying and permission to reprint should be submitted to CCC at www.copyright.com; employ the eISSN 1533-3884 to initiate your request. See also AIAA Rights and Permissions www.aiaa.org/randp.

*Ph.D. Candidate, School of Automation Science and Electrical Engineering; yangkun_buaa@buaa.edu.cn.

†Professor, School of Automation Science and Electrical Engineering; bcg@buaa.edu.cn.

‡Professor, School of Automation Science and Electrical Engineering; qq_buaa@buaa.edu.cn (Corresponding Author).



a) Interceptable **b) Uninterceptable**

Fig. 1 Motivation example: two scenarios of interception.

II. Model and Problem Formulation

In this section, a six-degree-of-freedom (6-DOF) rigid model of the interceptor and the visual servo model is proposed. With them, the interception feasibility problem is formulated.

A. Coordinate Systems and Models

1. Coordinate Systems

The coordinate systems are depicted in Fig. 2. The Earth-fixed coordinate system (EFCS), whose basis is composed of the column vectors of the identity matrix $[\boldsymbol{e}_1\ \ \boldsymbol{e}_2\ \ \boldsymbol{e}_3]$, is chosen as the inertial frame. The body coordinate system (BCS) is made up of an orthonormal basis $\{x_b, y_b, z_b\}$, with the origin located at the interceptor's center of mass. The camera coordinate system (CCS) is made up of an orthonormal basis $\{x_c, y_c, z_c\}$, with the origin located at the optical center of the camera. The image coordinate system (ICS) is made up of an orthonormal basis $\{x_i, y_i\}$, with the origin at the center of the image. The target coordinate system (TCS) is made up of an orthonormal basis $\{x_t, y_t, z_t\}$ and is used to represent the position and velocity of the interceptor relative to the target (intruder). The plane composed of $\boldsymbol{n}_t$ and ${}^e\boldsymbol{v} - {}^e\boldsymbol{v}_t$ is defined as the $x_t - z_t$ plane, where ${}^e\boldsymbol{v}$ and ${}^e\boldsymbol{v}_t$ are the velocities of the interceptor and target, respectively, as detailed in the next subsection. TCS is a noninertial system, its origin moves with the target, the x_t axis is collinear with vector $\boldsymbol{n}_t$ in the same direction, the z_t axis is perpendicular to the x_t axis on the $x_t - z_t$ plane, and the y_t axis is determined according to the right-hand rule.

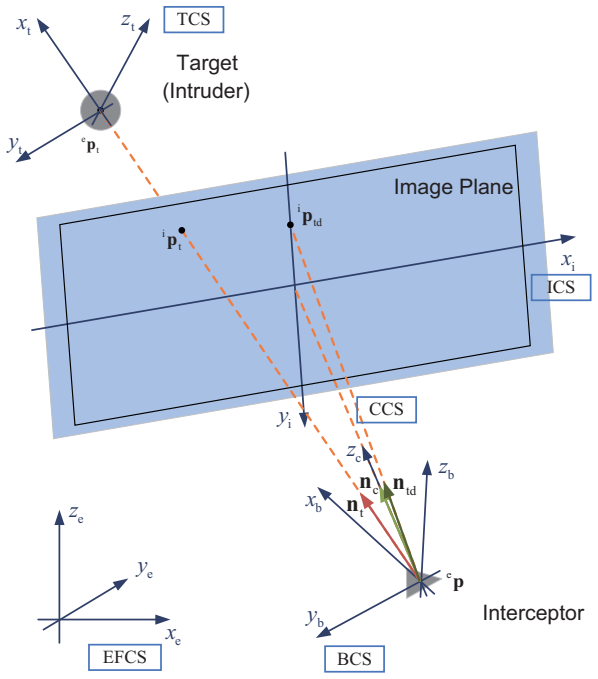


Fig. 2 Description of the interception problem.

The interception problem is illustrated in Fig. 2, where vectors ${}^e\boldsymbol{p}$ and ${}^e\boldsymbol{p}_t$ represent the positions of the interceptor and the target in EFCS, respectively. The coordinate of the target in the ICS is denoted as ${}^i\boldsymbol{p}_t = [p_{x_i}\ \ p_{y_i}]^T$. The unit vector along the LOS in EFCS is represented by $\boldsymbol{n}_t$, while the optical axis unit vector in EFCS is denoted by $\boldsymbol{n}_c$. The unit vector of the designed LOS in EFCS, called the designed LOS vector, is represented by $\boldsymbol{n}_{td}$. The intersection of $\boldsymbol{n}_{td}$ with the image plane in ICS, known as the intercept point, is represented by ${}^i\boldsymbol{p}_{td}$. The interception problem can be summarized as ensuring that $\boldsymbol{n}_t$ and $\boldsymbol{n}_{td}$ are collinear so that ${}^e\boldsymbol{p}$ and ${}^e\boldsymbol{p}_t$ are close to each other.

Throughout this Note, superscripts $({}^F\boldsymbol{r})(F = \{e\}, \{b\}, \{c\}, \{i\}, \{t\})$ are used to specify in which coordinate system a three-dimensional vector $\boldsymbol{r}$ is formulated. For simplicity, vectors in TCS can omit this superscript. Matrix $\boldsymbol{R}_{F_1}^{F_2}$ represents a rotation matrix from coordinate system F_1 to F_2, $\boldsymbol{R}_{F_1}^{F_2} \in \mathrm{SO}(3)$, where the three-dimensional special orthogonal group is given by $\mathrm{SO}(3) = \{\boldsymbol{R} \in \mathbb{R}^{3\times3} \mid \boldsymbol{R}^T\boldsymbol{R} = \boldsymbol{I}, \det(\boldsymbol{R}) = 1\}$.

2. Target Model

The target's motion is represented using a point-mass model as

$$\begin{cases} {}^e\dot{\boldsymbol{p}}_t = {}^e\boldsymbol{v}_t \\ {}^e\dot{\boldsymbol{v}}_t = {}^e\boldsymbol{g} + {}^e\boldsymbol{a}_t \end{cases} \tag{1}$$

where ${}^e\boldsymbol{p}_t \in \mathbb{R}^3$, ${}^e\boldsymbol{v}_t \in \mathbb{R}^3$, and ${}^e\boldsymbol{a}_t \in \mathbb{R}^3$ are the target's position, velocity, and thrust acceleration in EFCS, respectively. The control input of the target, ${}^e\boldsymbol{a}_t$, is unknown to the interceptor. Vector ${}^e\boldsymbol{g}$ represents the local gravitational acceleration in EFCS, defined as ${}^e\boldsymbol{g} = [0\ \ 0\ \ g]^T$, with $g = 9.81\ \mathrm{m/s^2}$. The thrust-to-weight ratio of the target, τ_t, is defined as the ratio of the target's thrust acceleration to the gravitational acceleration, given by $\tau_t = \|{}^e\boldsymbol{a}_t\|/g$. The maximum thrust-to-weight ratio of the target is denoted as $\tau_{t,\max}$, with the constraint $\tau_t \le \tau_{t,\max}$.

3. Interceptor Model

The interceptor's attitude is represented by a rotation matrix, and its flight control rigid model [29] is summarized as

$$\begin{cases} {}^e\dot{\boldsymbol{p}} = {}^e\boldsymbol{v} \\ {}^e\dot{\boldsymbol{v}} = {}^e\boldsymbol{g} + \dfrac{1}{m}{}^e\boldsymbol{f} \\ \dot{\boldsymbol{R}}_b^e = \boldsymbol{R}_b^e[{}^b\omega]_\times \end{cases} \tag{2}$$

where ${}^e\boldsymbol{p} \in \mathbb{R}^3$ and ${}^e\boldsymbol{v} \in \mathbb{R}^3$ are the interceptor's position and velocity in EFCS, respectively; m is the mass of the interceptor; and ${}^e\boldsymbol{f} \in \mathbb{R}^3$ is the control input of the interceptor in EFCS. The angular velocity in BCS is denoted by ${}^b\omega \in \mathbb{R}^3$, and $[{}^b\omega]_\times$ is a skew-symmetric matrix ([29], Chap. 5), which serves as a cross-product map of the angular velocity ${}^b\omega$.

Downloaded by BEIHANG UNIVERSITY on March 30, 2025 | http://arc.aiaa.org | DOI: 10.2514/1.G008527

Downloaded by BEIHANG UNIVERSITY on March 30, 2025 | http://arc.aiaa.org | DOI: 10.2514/1.G008527

The cross-product map $[\cdot]_\times$: $\mathbb{R}^3 \to \mathfrak{so}(3)$ is defined such that $[\boldsymbol{x}]_\times \boldsymbol{y} = \boldsymbol{x} \times \boldsymbol{y}$ and $[\boldsymbol{x}]_\times^T = -[\boldsymbol{x}]_\times$ for any $\boldsymbol{x}, \boldsymbol{y} \in \mathbb{R}^3$, where the set of 3 by 3 skew-symmetric matrices is denoted by $\mathfrak{so}(3) = \{\boldsymbol{S} \in \mathbb{R}^{3\times3} \mid \boldsymbol{S} = -\boldsymbol{S}^T\}$. For $\boldsymbol{x} \triangleq [x_1 \;\; x_2 \;\; x_3]^T \in \mathbb{R}^3$, the cross product map is summarized as

$$[\boldsymbol{x}]_\times \triangleq \begin{bmatrix} 0 & -x_3 & x_2 \\ x_3 & 0 & -x_1 \\ -x_2 & x_1 & 0 \end{bmatrix}$$

Considering the intrusion target's movement, the interceptor's flight control rigid model in TCS is

$$\begin{cases} \dot{\boldsymbol{p}} = \boldsymbol{v} \\ \dot{\boldsymbol{v}} = \dfrac{1}{m}\boldsymbol{f} - \boldsymbol{a}_t + \dfrac{1}{m}\boldsymbol{f}_{\text{fic}} \\ \dot{\boldsymbol{R}}_t^e = \boldsymbol{R}_t^e[\omega_T]_\times \end{cases} \tag{3}$$

where $\boldsymbol{p} \in \mathbb{R}^3$ is the position of the interceptor in TCS, $\boldsymbol{p} = \boldsymbol{R}_t^{eT}({}^e\boldsymbol{p} - {}^e\boldsymbol{p}_t)$; $\boldsymbol{v} \in \mathbb{R}^3$ is the velocity of the interceptor in TCS, $\boldsymbol{v} = \boldsymbol{R}_t^{eT}({}^e\boldsymbol{v} - {}^e\boldsymbol{v}_t) - \omega_T \times \boldsymbol{p}$; ω_T is the angular velocity of the rotating reference frame TCS relative to EFCS; $\boldsymbol{a}_t$ is the control input of the target in TCS, $\boldsymbol{a}_t = \boldsymbol{R}_t^{eTe}\boldsymbol{a}_t$; $\boldsymbol{f} \in \mathbb{R}^3$ is the control input of the interceptor in TCS, $\boldsymbol{f} = \boldsymbol{R}_t^{eTe}\boldsymbol{f}$, called the controllable force; $\boldsymbol{f}_{\text{fic}} = m(-{}^e\dot{\omega}_T \times \boldsymbol{p} - 2\omega_T \times \boldsymbol{v} - \omega_T \times (\omega_T \times \boldsymbol{p}))$ represents the fictitious force generated by the rotation of TCS relative to EFCS, including Euler force, Coriolis force, and centrifugal force ([30], Chap. 5); $\boldsymbol{f}_{\text{unc}} = -m\boldsymbol{a}_t + \boldsymbol{f}_{\text{fic}}$ represents the uncontrollable force of the interceptor in TCS. The detailed derivations are placed in the Appendix. The interceptor is subjected to the net force $\boldsymbol{f}_{\text{net}} = \boldsymbol{f} + \boldsymbol{f}_{\text{unc}}$.

The pursuit–evasion game means that the control inputs of the interceptor must take into account the control inputs of the target, effectively finding the optimal control for the interceptor under the worst-case action by the target. This Note considers multicopters as interceptors. The controllable force generated by the thrust of the propellers is given by

$$\boldsymbol{f} = f\boldsymbol{R}_b^t\boldsymbol{R}_f\boldsymbol{e}_3 \tag{4}$$

where $0 \le f \le f_m$, and f_m is the maximum thrust. The maximum thrust-to-weight ratio of the interceptor is defined as $\tau_{\max} = f_m/g$. The rotation matrix $\boldsymbol{R}_f \in \mathsf{SO}(3)$ transforms the thrust vector to z_b axis in BCS. For multicopters, $\boldsymbol{R}_f$ is constant because the propellers provide thrust in a fixed direction relative to the fuselage, while for tiltrotor aircrafts, $\boldsymbol{R}_f$ is variable [31]. Vector $\boldsymbol{e}_3$ is the third column of the 3×3 identity matrix, $\boldsymbol{e}_3 = [0 \;\; 0 \;\; 1]^T$.

4. Camera Imaging Model

As shown in Fig. 2, the perspective projection maps from three-dimensional space to the two-dimensional image plane: $\mathbb{R}^3 \to \mathbb{R}^2$.

Assumption 1: The origin of CCS coincides with the origin of BCS. That is, their translation vector $\boldsymbol{t}_c^b = \boldsymbol{0}$, and rotation matrix $\boldsymbol{R}_c^b$ is constant.

When the target is within the sensor's FOV, vector $\boldsymbol{n}_t$ is obtained through a unified imaging model ([32], Chap. 11) using the image coordinates and the focal length f_{oc} as

$$\begin{aligned} \boldsymbol{n}_t &= -\frac{\boldsymbol{p}}{\|\boldsymbol{p}\|} \\ &= \boldsymbol{R}_b^e\boldsymbol{R}_c^b\frac{[p_{x_i} \;\; p_{y_i} \;\; f_{\text{oc}}]^T}{\left\|[p_{x_i} \;\; p_{y_i} \;\; f_{\text{oc}}]^T\right\|} \end{aligned} \tag{5}$$

The FOV is the range of the observable area that a perception sensor can image, including the horizontal field of view (HFOV) and vertical field of view (VFOV). The parameters α_{hfov} and α_{vfov} represent the angles of HFOV and VFOV of the perception sensor. The FOV is mathematically defined as $\mathcal{C} = \{\boldsymbol{x} \mid |\arctan(x_{c1}/x_{c3})| \le (1/2)\alpha_{\text{hfov}}, |\arctan(x_{c2}/x_{c3})| \le (1/2)\alpha_{\text{vfov}}\}$, where ${}^c\boldsymbol{x} \triangleq [x_{c1} \;\; x_{c2} \;\; x_{c3}]^T$ represents $\boldsymbol{x}$ in CCS. To avoid the target being too close to the edge of the sensor's FOV, the practical FOV angles are defined as α'_{hfov} and α'_{vfov}. The corresponding FOV is $\mathcal{C} = \{\boldsymbol{x} \mid |\arctan(x_{c1}/x_{c3})| \le (1/2)\alpha'_{\text{hfov}}, |\arctan(x_{c2}/x_{c3})| \le (1/2)\alpha'_{\text{vfov}}\}$.

The camera imaging is subject to the LOS constraint that the target is within the sensor's FOV:

$$\boldsymbol{n}_t \in \mathcal{C} \tag{6}$$

B. Problem Formulation

For simplicity, only the control problem is considered first.

Definition 1: Dynamic system (3) is said to be *interceptable* if for every initial condition $\boldsymbol{p}(t_0)$, $\boldsymbol{v}(t_0)$ there exists a finite time $t_f > t_0$ and control $\boldsymbol{u}(t), t \in [t_0, t_f]$ to transfer the system state $\boldsymbol{p}(t_f) = \boldsymbol{0}$.

Moreover, the interceptability considering the sensor imaging is defined as follows:

Definition 2: Dynamic system (3) is said to be globally LOS-constrained interceptable if for every initial condition $\boldsymbol{p}(t_0) \in \mathcal{C}$, $\boldsymbol{v}(t_0)$ there exists a finite time $t_f > t_0$ and control $\boldsymbol{u}(t), t \in [t_0, t_f]$ to transfer the system state $\boldsymbol{p}(t_f) = \boldsymbol{0}$; meanwhile, LOS condition (6) holds.

Definition 1 describes the transition of a system from an initial state to a specific state in finite time, which can be regarded as a substate or output reachability problem [33]. It can be shown that a linear system is reachable if and only if the acceleration capability of the interceptor is greater than that of the target. In the actual interception task, the LOS constraint, namely, keeping the target within the FOV of the sensor, must be considered. Whether a system is interceptable with the LOS constraint is summarized in Definition 2. Nonlinearity makes the problem challenging.

Based on the above assumptions and definitions, the controller problem is summarized as follows.

1. Feasibility Problem

Aim at finding $\boldsymbol{n}_{td}, \boldsymbol{f}_d$, so that dynamic system (3) is globally LOS-constrained interceptable with $\boldsymbol{n}_t = \boldsymbol{n}_{td}$ and $\boldsymbol{f} = \boldsymbol{f}_d$. Furthermore, define and measure the DOI of dynamic system (3).

This study follows the principle of separating the configuration design of the interceptor from its control. We assume that the controller can rapidly respond to the designed $\boldsymbol{n}_{td}$ and $\boldsymbol{f}_d$, thereby computing the interceptability. In practical applications of our previous work [9,10], the controller is responsible for achieving $\boldsymbol{n}_t \to \boldsymbol{n}_{td}$ and $\boldsymbol{f} \to \boldsymbol{f}_d$. This Note focuses on evaluating the interceptor configuration and designing the LOS vector under perfect control conditions.

Since some states cannot be obtained, such as the target motion acceleration $\boldsymbol{a}_t$, the interceptor cannot be controlled simply according to the thrust and attitude obtained in the feasibility problem. Practically, based on the previously designed $\boldsymbol{n}_{td}$, a controller needs to be designed to complete the interception task using only its image observation and IMU information feedback.

III. Interceptability

In this section, to solve the feasibility problem, the interceptability is analyzed, which is about a measure of an interceptor configuration but not the interception controller. The interceptability guides the design of the interceptor configuration to make interception tasks easier to perform.

A. Degree of Interceptability Theory

The interceptability definitions and various interceptability scenarios are depicted in Fig. 3. For the interceptability of 6-DOF rigid bodies illustrated in Fig. 3a, λ represents the angle between the designed controllable force $\boldsymbol{f}_d$ and the designed LOS vector $\boldsymbol{n}_{td}$. Similarly, μ represents the angle between the uncontrollable force

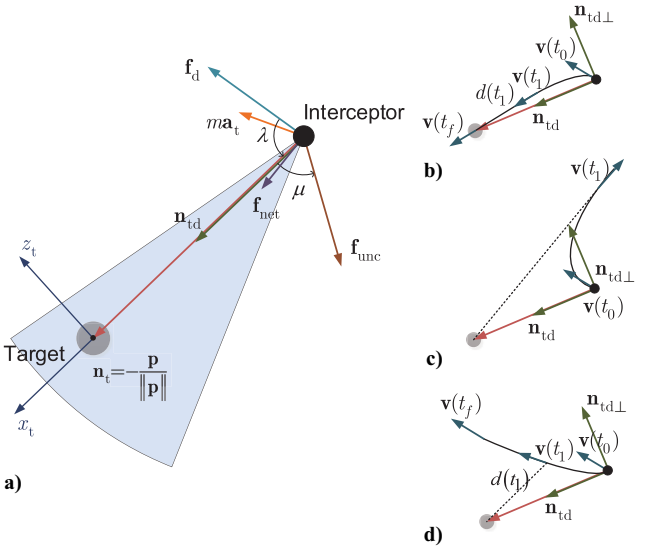


Fig. 3 Interceptability of 6-DOF rigid bodies and different interceptability situations.

$\boldsymbol{f}_{\text{unc}}$ and the designed LOS vector $\boldsymbol{n}_{td}$, which is primarily related to the direction of the target's acceleration. The definition domain of μ is denoted as $\mathcal{M}$.

To formulate easily computable algebraic interceptability criteria, the DOI is introduced to measure the interception capability of the interceptor. It can be formulated as a pursuit–evasion game and modeled with a constrained minimax problem.

Definition 3: DOI is a measure of the intercepting ability of dynamic system (3) where LOS condition (6) holds. The DOI is defined as

$$I = \min_{\boldsymbol{a}_t} \max_{\boldsymbol{n}_{td}, \boldsymbol{f}_d} \frac{\boldsymbol{n}_{td}^T \boldsymbol{f}_{\text{net}}}{\tau_{t,\max} mg} \tag{7}$$

$$\text{s.t.} \quad \Omega(0,\varepsilon) \subseteq \frac{1}{m}\boldsymbol{e}_3^T \boldsymbol{f}_{\text{net}} \tag{7a}$$

$$\boldsymbol{n}_{td} \in \mathcal{C} \tag{7b}$$

$$\|\boldsymbol{f}_d\| \le f_m, \boldsymbol{R}_f \in \Omega_R \tag{7c}$$

$$\|\boldsymbol{a}_t\| \le \tau_{t,\max} g, \boldsymbol{n}_{td}^T \boldsymbol{a}_t \le 0 \tag{7d}$$

for an existing neighborhood $\Omega(0,\varepsilon)$ denoted by $\Omega(0,\varepsilon) = \{x \in \mathbb{R} \mid |x| < \varepsilon\}, \varepsilon > 0$. Set Ω_R is a subset of $\mathsf{SO}(3)$ and represents the range of values for $\boldsymbol{R}_f$. When the constraints are not satisfied, set $I = -\infty$.

The definition and constraints of I include the following: Equation (7) indicates the maximum acceleration that the interceptor can achieve in the direction of the LOS vector when the target adopts the optimal strategy, and then normalizes it by dividing it by its own maximum acceleration. Constraint (7a) indicates that net force $\boldsymbol{f}_{\text{net}}$ is collinear with $\boldsymbol{n}_{td}$ even if the target adopts optimal strategy $\boldsymbol{a}_t$. Constraint (7b) indicates that designed LOS vector $\boldsymbol{n}_{td}$ is within the FOV, which varies with different types of perception sensors. Constraint (7c) indicates that the magnitude of thrust $\boldsymbol{f}_d$ is not greater than the maximum thrust f_m. Constraint (7d) indicates that the target acceleration is constrained by its maximum thrust-to-weight ratio. The interceptor is deployed in the direction of the target's intrusion.

In typical pursuit–evasion games [20], the evader's goal is to maximize the time to capture, while the pursuer aims to minimize it. In contrast, in Eq. (7), the target seeks to minimize the interceptability metric, making it harder to intercept, while the interceptor maximizes this metric to enhance its intercept capabilities. This distinction reflects the focus on system design rather than dynamic strategy optimization during the pursuit process.

The application of the DOI is introduced in Sec. III.C. Further study of the DOI leads to the following results: Lemma 1, the coplanarity of optimal policies, and Theorem 1, the relationship between the DOI and global interceptability.

Lemma 1: The optimal strategies $\boldsymbol{a}_t^*$ and $\boldsymbol{f}_d^*$ of the target and interceptor are both on $\boldsymbol{v}$–$\boldsymbol{n}_{td}$ plane, which is defined as the plane composed of $\boldsymbol{v}$ and $\boldsymbol{n}_{td}$.

Proof: The solution to a DOI is divided into two steps. First, for any $\boldsymbol{a}_t$ satisfying constraint (7d), the corresponding strategies $\boldsymbol{f}_d^*(\boldsymbol{a}_t)$ and $\boldsymbol{n}_{td}^*(\boldsymbol{a}_t)$ of interceptors that satisfy constraints (7a–7c) are obtained as

$$\begin{aligned} &\boldsymbol{n}_{td}^*(\boldsymbol{a}_t), \boldsymbol{f}_d^*(\boldsymbol{a}_t) = \arg\max_{\boldsymbol{n}_{td}, \boldsymbol{f}_d} I(\boldsymbol{n}_{td}, \boldsymbol{f}_d \mid \boldsymbol{a}_t) \\ &\text{s.t.} \quad \text{(7a), (7b), (7c), (7d)} \end{aligned} \tag{8}$$

Then, the target selection strategy minimizes the DOI, and the corresponding $\boldsymbol{f}_d^*(\boldsymbol{a}_t)$ is denoted as $\boldsymbol{f}_d^*$. The optimal strategy of the target is

$$\begin{aligned} &\boldsymbol{a}_t^* = \arg\min_{\boldsymbol{a}_t} I\big(\boldsymbol{a}_t \mid \boldsymbol{n}_{td}^*(\boldsymbol{a}_t), \boldsymbol{f}_d^*(\boldsymbol{a}_t)\big) \\ &\text{s.t.} \quad \text{(7a), (7b), (7c), (7d)} \end{aligned} \tag{9}$$

The optimal strategy pair of the target and interceptor $(\boldsymbol{a}_t^*, \boldsymbol{f}_d^*)$ is an equilibrium point in this pursuit–evasion game. Neither party can increase their expected payoff by changing their strategy while the other party's strategy remains unchanged.

The normal component of vector $\boldsymbol{x}$ is defined as $\boldsymbol{x}_\perp$, $\boldsymbol{x}_\perp \triangleq \boldsymbol{x} - \boldsymbol{n}_{td}^T \boldsymbol{x} \boldsymbol{n}_{td}$. By constraint (7a) in Eq. (9), for a given $\varepsilon > 0$, the target's optimal strategy is to maximize $\|(1/m)\boldsymbol{f}_{\text{unc}\perp} + \varepsilon \boldsymbol{v}_\perp\|$. According to the definition of the normal component $\boldsymbol{x}_\perp$, we have

$$\begin{aligned} \left\| \frac{1}{m}\boldsymbol{f}_{\text{unc}\perp} + \varepsilon \boldsymbol{v}_\perp \right\| &\le \left\| \frac{1}{m}\boldsymbol{f}_{\text{unc}\perp} \right\| + \varepsilon \|\boldsymbol{v}_\perp\| \\ &= \left\| \frac{1}{m}\boldsymbol{f}_{\text{fic}\perp} - \boldsymbol{a}_{t\perp} \right\| + \varepsilon \|\boldsymbol{v}_\perp\| \\ &\le \|\boldsymbol{a}_{t\perp}\| + \left\| \frac{1}{m}\boldsymbol{f}_{\text{fic}\perp} \right\| + \varepsilon \|\boldsymbol{v}_\perp\| \end{aligned}$$

The equality holds if and only if $\boldsymbol{a}_{t\perp}$, $\boldsymbol{f}_{\text{fic}\perp}$, and $\boldsymbol{v}_\perp$ are collinear. According to the definition of $\boldsymbol{f}_{\text{fic}}$, $\boldsymbol{f}_{\text{fic}}$ is on the $\boldsymbol{v}$–$\boldsymbol{n}_{td}$ plane; therefore, $\boldsymbol{a}_t^*$ is also on this plane. □

Lemma 1 shows that the optimal strategies are on the same plane, thus reducing the three-dimensional interception problem to a two-dimensional plane scenario. In the simulation section, it is verified that the target adopts other strategies to make it intercepted in a shorter time.

Theorem 1: If and only if $I > 0$, then dynamic system (3) is globally LOS-constrained interceptable with constraint (6).

Proof: 1) Condition conversion: According to Lemma 1, the optimal strategies $\boldsymbol{a}_t^*$ and $\boldsymbol{f}_d^*$ for the target and interceptor both lie on the $\boldsymbol{v}$–$\boldsymbol{n}_{td}$ plane. Hence, only convergence on this plane needs to be considered. From Definition 2, the theorem is equivalently stated as follows: For dynamic system (3) with observation models (5) and (6), if and only if $I > 0$ then for all $\boldsymbol{p}(t_0)$ and $\boldsymbol{v}(t_0)$, there exist a finite time $t_f > t_0$ and control $\boldsymbol{u}(t), t \in [t_0, t_f]$ to transfer the distance between the interceptor and target $\boldsymbol{p}(t_f) = \boldsymbol{0}$.

2) Proof of sufficiency: Assume $I > 0$, so the constraint (7a) holds under LOS and maximum thrust constraints. Along x_t and z_t directions, dynamic system (3) decomposes into horizontal and vertical subsystems as

$$\begin{cases} \dot{v}_x = \boldsymbol{n}_{td}^T \dot{\boldsymbol{v}} \\ \dot{v}_z = \boldsymbol{e}_3^T \dot{\boldsymbol{v}} \end{cases}$$

From the null-controllable theory ([34], Theorem 1.1) [35], if there exists a set $\Omega(0,\varepsilon) \subseteq \mathbb{R}^3$ containing $u = \dot{v}_z = 0$ in its interior, the vertical subsystem is null-controllable. This implies that a bounded admissible control $u(t)$, defined on some finite interval $t_0 \le t \le t_1$,

Downloaded by BEIHANG UNIVERSITY on March 30, 2025 | http://arc.aiaa.org | DOI: 10.2514/1.G008527

Downloaded by BEIHANG UNIVERSITY on March 30, 2025 | http://arc.aiaa.org | DOI: 10.2514/1.G008527

can steer v_z to 0. Given that constraint (7a) holds, the subsystem in the z_t direction stabilizes at the equilibrium point 0.

As shown in Fig. 3b, suppose that, at time $t_1 > t_0$, $\boldsymbol{v}$ is collinear with $\boldsymbol{n}_{td}$, i.e., $v_z(t_1) = 0$. At this time, TCS no longer rotates relative to the inertial system, and the acceleration aligns with $\boldsymbol{n}_{td}$, $\dot{\boldsymbol{v}} = (1/m)\boldsymbol{f}_d - \boldsymbol{a}_t$. Consequently, the interceptor approaches the target with uniform acceleration, and the total interception time is $t_f = t_1 + [1/\dot{v}_x(t_1)](\sqrt{v_x^2(t_1) + \dot{v}_x(t_1)p_x(t_1)} - v_x(t_1))$.

3) Proof of necessity: The necessary condition is proved by contraposition: if $I \le 0$, the distance between the interceptor and target cannot reduce to zero in finite time. The condition $I \le 0$ encompasses two cases.

Case 1: As shown in Fig. 3c, the LOS and maximum thrust constraints are satisfied, but $\boldsymbol{n}_{td}^T\dot{\boldsymbol{v}} \le 0$. Assume that at time $t_1 > t_0$, $\boldsymbol{v}$ is collinear with $\boldsymbol{n}_{td}$, $v_z(t_1) = 0$. However, acceleration $\dot{v}_x$ opposite to the designed LOS vector will cause the interceptor to move away from the target, $p_x(t) = p_x(t_1) + v_x(t_1)t + (1/2)\dot{v}_x(t_1)t^2 \to -\infty$, making interception impossible.

Case 2: As shown in Fig. 3d, constraint (7a) is not satisfied, $\Omega(0, \varepsilon) \nsubseteq \boldsymbol{n}_{td\perp}^T\dot{\boldsymbol{v}}$, so $\boldsymbol{v}$ cannot be collinear with $\boldsymbol{n}_{td}$ under LOS and maximum thrust constraints. The target adopts the optimal strategy $\boldsymbol{a}_t^*$, and then in z_t direction, $v_z(t) = \int_{t_0}^{t} \boldsymbol{n}_{td\perp}^T\dot{\boldsymbol{v}}\,\mathrm{d}t \ge v_z(t_0)$, and $d(t) \ge d(t_0)$ for $t > t_0$. Thus, the target can use a control strategy that prevents the interceptor from successfully intercepting it.

Proofs of cases 1 and 2 conclude the proof of necessity. □

B. Analytical Criteria of the DOI in Practice

The solution to the DOI is obtained by solving Eqs. (8) and (9) sequentially. First, the key to solving Eq. (8) is finding the optimal strategies for the interceptor $\boldsymbol{f}_d^*(\boldsymbol{a}_t)$ and $\boldsymbol{n}_{td}^*(\boldsymbol{a}_t)$. This is equivalent to determining the magnitude of the controllable force $\|\boldsymbol{f}_d^*\|$ and the angle λ^* between the controllable force and the designed LOS vector $\boldsymbol{n}_{td}$. Constraint (7a) is equivalent to $\Omega(0, \varepsilon) \subseteq \{\|\boldsymbol{f}_d\| \sin\lambda - \|\boldsymbol{f}_{\mathrm{unc}}\| \sin\mu \mid \mu \in \mathcal{M}\}$. For any feasible target strategy, the minimum feasible value of $\lambda_{\min} = \arcsin((\|\boldsymbol{f}_{\mathrm{unc}}\| \sin\mu + \varepsilon)/f_m)$. The minimum feasible value that satisfies constraint (7) is λ_{fov}. Therefore, the minimum angle between the controllable force $\boldsymbol{f}_d$ and the designed LOS vector $\boldsymbol{n}_{td}$ in a feasible interceptor configuration is $\lambda^* = \max(\lambda_{\min}, \lambda_{\mathrm{fov}})$. Thus, $\boldsymbol{f}_d^*(\boldsymbol{a}_t)$ and $\boldsymbol{n}_{td}^*(\boldsymbol{a}_t)$ are determined. If constraint (7a) is still not satisfied, the interceptor is uninterceptable due to practical constraints.

Next, solving Eq. (9) involves finding the target's optimal strategy $\boldsymbol{a}_t^*$, which is equivalent to determining the magnitude of the uncontrollable force $\|\boldsymbol{f}_{\mathrm{unc}}^*\|$ and the angle μ^* between the uncontrollable force and the LOS vector. In the system's steady state, when the angle between the uncontrollable force $\boldsymbol{f}_{\mathrm{unc}}$ and the LOS vector $\boldsymbol{n}_{td}$ is μ, we have $\|\boldsymbol{f}_d\| = \|\boldsymbol{f}_{\mathrm{unc}}\|(\sin\mu/\sin\lambda^*)$. At this point, the net force $\boldsymbol{f}_{\mathrm{net}}$ and the LOS vector $\boldsymbol{n}_{td}$ are collinear, and $\|\boldsymbol{f}_{\mathrm{net}}\| = \|\boldsymbol{f}_{\mathrm{unc}}\|(\cos\mu + \sin\mu\cot\lambda^*)$. The target adopts maximum acceleration $\tau_{t,\max}mg$ and the optimal strategy μ^* to minimize the net force. By combining these, we can derive the target's optimal strategy $\boldsymbol{a}_t^*$, and, accordingly, the interceptor's optimal strategies $\boldsymbol{f}_d^*(\boldsymbol{a}_t^*)$ and $\boldsymbol{n}_{td}^*(\boldsymbol{a}_t^*)$ are also determined.

Considering the power and camera configuration of the interceptor in practice, the DOI is a measure of the intercept capability of dynamic system (3) under LOS condition (6). For an interceptor, the DOI is calculated as

$$I = \frac{\|\boldsymbol{f}_{\mathrm{unc}}^*\|(\cos\mu^* + \sin\mu^*\cot\lambda^*)}{\tau_{t,\max}mg} \tag{10}$$

Equation (10) provides an analytical criterion rather than an optimization problem as in Theorem 1. In the next subsection, specific design recommendations are provided based on the characteristics of the multicopter.

C. Multicopter Design Guidelines

When utilizing a multicopter as an interceptor, the different interceptable cases are illustrated in Fig. 4. In Fig. 4a, common cameras have a limited FOV as shown in region I; gimbal cameras have a variable FOV as shown in region II; and panoramic cameras and omni-directional LiDAR have a 360° FOV as shown in region III. Several key angles are defined as follows: $\beta \in [-(\pi/2), (\pi/2)]$ represents the angle between the designed controllable force $\boldsymbol{f}_d$ and the z_b axis; $\gamma \in [-(\alpha_{\mathrm{fov}}/2), (\alpha_{\mathrm{fov}}/2)]$ represents the angle between the designed LOS vector $\boldsymbol{n}_{td}$ and the optical axis unit vector $\boldsymbol{n}_c$, which varies with the designed LOS vector; $\delta_c \in [-(\pi/2), (\pi/2)]$ represents the angle between the optical axis unit vector $\boldsymbol{n}_c$ and the plane of the fuselage, indicating the camera installation angle. If the multicopter is equipped with a strapdown camera, δ_c remains constant. The propellers generate thrust in a direction fixed relative to the fuselage, making $\boldsymbol{R}_f$ constant. The angle λ^* guides the multicopter configuration design, requiring $\lambda_d > \lambda^*$ or $\lambda_d < -\lambda^*$.

1. *Feasible DOI, $I > 0$*

According to the geometric relationship, λ_d should satisfy $\lambda_d = (\pi/2) + \delta_c - \beta - \gamma$. As illustrated in Fig. 4b, the interceptor locks onto the target and accelerates along the designed LOS vector. The following design considerations emerge from analyzing the multicopter configuration parameters:

1) The thrust must have a forward acceleration component; a larger β facilitates interception tasks.

2) The designed LOS vector should be upward relative to the optical axis direction, implying $\gamma > 0$.

3) The camera should be installed facing upward, indicating $\delta_c < 0$.

Furthermore, when $\lambda_d = \lambda_{\min}$, I reaches its maximum value, $I_{\max} = (f_m/\tau_{t,\max}mg) = (\tau_{\max}/\tau_{t,\max})$. At this point, the thrust is sufficiently aligned with the optical axis and sufficiently strong. Therefore, to achieve the theoretical maximum DOI, a multicopter should be designed with its thrust direction aligned with the optical axis and a high thrust-to-weight ratio. This design principle is similar to the propulsion and sensor configuration of missiles. In summary, besides the aforementioned recommendations, installing a camera aligned with the thrust direction can help achieve the theoretical maximum DOI.

2. *Infeasible DOI, $I \le 0$*

In Fig. 4c, the multicopter fails to intercept the target because the constraints in Eq. (7) are unmet, and the net force does not align with the designed LOS vector. Two primary reasons typically account for this failure:

1) The interceptor's acceleration is insufficient compared to the target's escape acceleration, $f_m < \|\boldsymbol{f}_{\mathrm{unc}}\|$.

2) An unreasonable multicopter configuration results in $\lambda_d \ge (\pi/2)$, and $(\cos\mu^* + \sin\mu^*\cot\lambda_d) \le 0$.

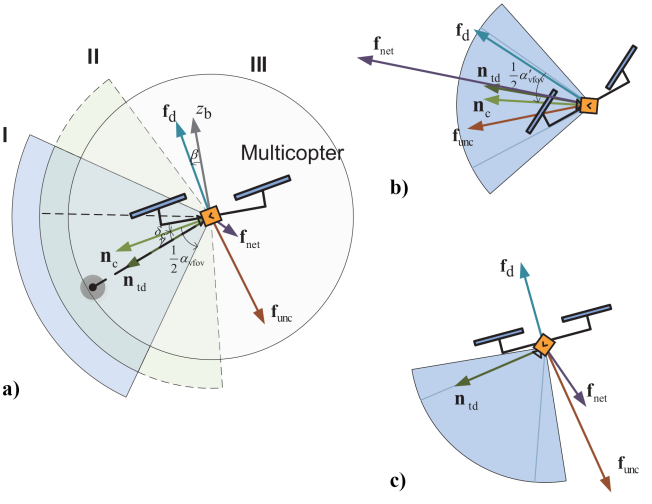


Fig. 4 Interceptability of multicopters.

Downloaded by BEIHANG UNIVERSITY on March 30, 2025 | http://arc.aiaa.org | DOI: 10.2514/1.G008527

IV. Numerical Simulation

This section illustrates the concept of interceptability using extensive Monte Carlo numerical simulations, which graphically represent the trajectories and statistical characteristics of interceptors under various DOI conditions. First, the simulations demonstrate that the DOI is calculated assuming both sides adopt optimal strategies, thereby verifying Lemma 1. It is shown that a target is intercepted more quickly when it deviates from the optimal strategy. Subsequently, simulations of interception efficacy across diverse multicopter configurations validate Theorem 1, establishing the DOI as a practical framework for interceptor configuration.

A. Illustrative Optimal Strategy

The computer simulation utilizes the interceptor model as defined by Eqs. (3–6). When both the interceptor and the target adopt optimal strategies, a positive interceptability index ($I > 0$) indicates that interception is feasible. Conversely, if the target deviates from the optimal strategy, the interceptor can achieve interception more rapidly.

The initial conditions within TCS are established as

$$\begin{aligned} \boldsymbol{p}(0) &= [-15 \;\; 10 \;\; 0]^T \text{ m}, \\ \boldsymbol{v}(0) &= [1 \;\; 0 \;\; -2]^T \text{ m/s} \end{aligned} \tag{11}$$

Table 1 Parameters of the optimal policy and spiral

Intrusion	$\boldsymbol{a}_t$	$\tau_{\max}$	$\tau_{t,\max}$	α_{vfov}, deg	α'_{vfov}, deg	β, deg	δ_c, deg
Optimal	Eq. (7)	2	1	120	90	30	0
Spiral	Eq. (12)	2	1	120	90	30	0

The target adopts a spiral motion to invade. Its acceleration is perpendicular to the axis, rotates counterclockwise, and always maintains the maximum acceleration capability as

$$\boldsymbol{a}_t(t) = \tau_{t,\max} g \boldsymbol{R}_x(10t)\boldsymbol{e}_3 \tag{12}$$

where $\boldsymbol{R}_x(\theta)$ represents the rotation matrix that rotates an angle $\theta \in \mathbb{R}$ around x_t axis. Additional parameters are detailed in Table 1.

It is assumed that both vehicles possess complete knowledge of the parameters necessary to execute their guidance strategies. The interceptor and target are launched simultaneously at the scenario's onset. The simulations are carried out to solve the differential equation and optimization using the Python scipy toolbox.

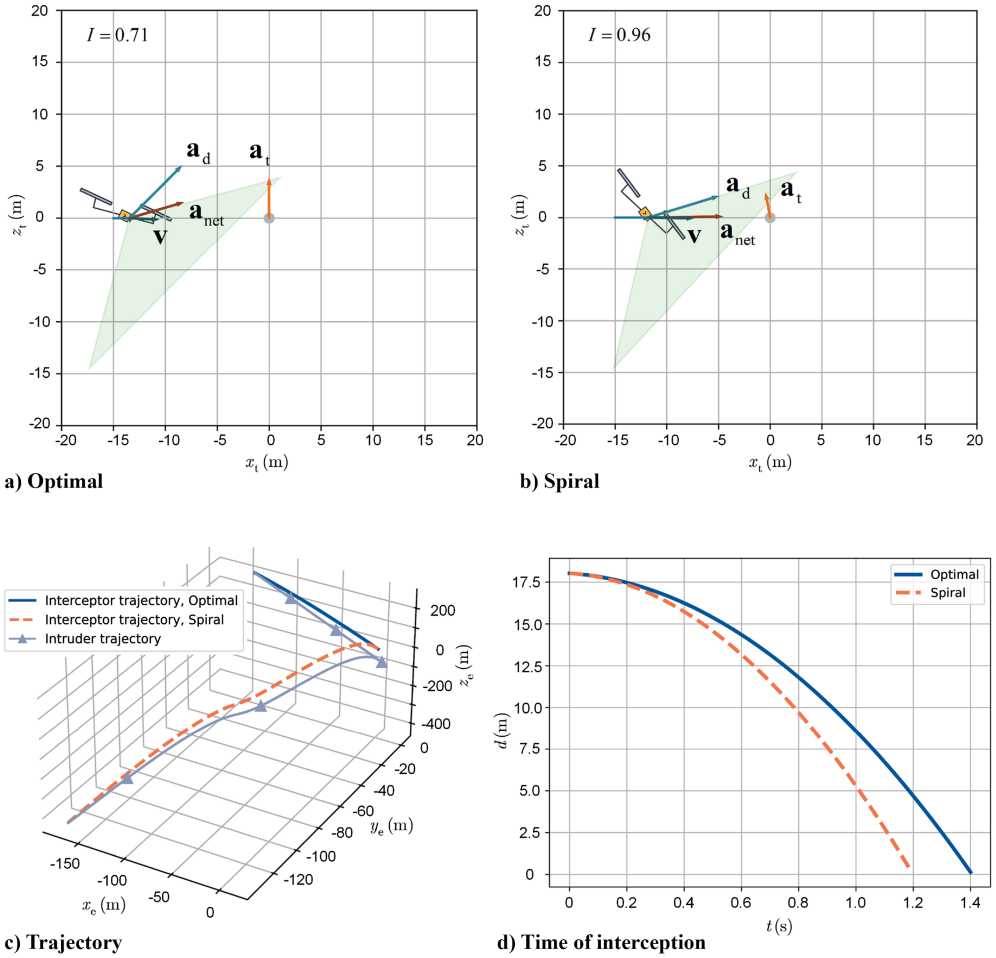
The miss distance [36] represents the minimal separation between the interceptor and its target, serving as a metric for interception precision. The simulations for both optimal and spiral strategies are terminated once the miss distance reaches 1 m, which is less than the physical dimensions of the entities involved.

Figures 5a and 5b depict the trajectories of the interceptor and target within TCS. Figure 5c shows the interception trajectories, and Fig. 5d shows the temporal variation of the distance between the interceptor and target. The target following the optimal strategy is intercepted at 1.68 s, whereas the target employing the spiral motion is intercepted more rapidly at 1.49 s. This highlights the validity of the DOI definition. The most challenging interception scenarios occur when the target employs its optimal strategy, and the DOI serves as a measure of the interceptor's capability in these exacting scenarios.

B. Examples of Interceptors

1. *DOI Measures the Interception Capability of the Interceptor*

The trajectories of the interceptor and target in both TCS and EFCS are shown in Figs. 6a–6c. The initial position of interceptors is set to

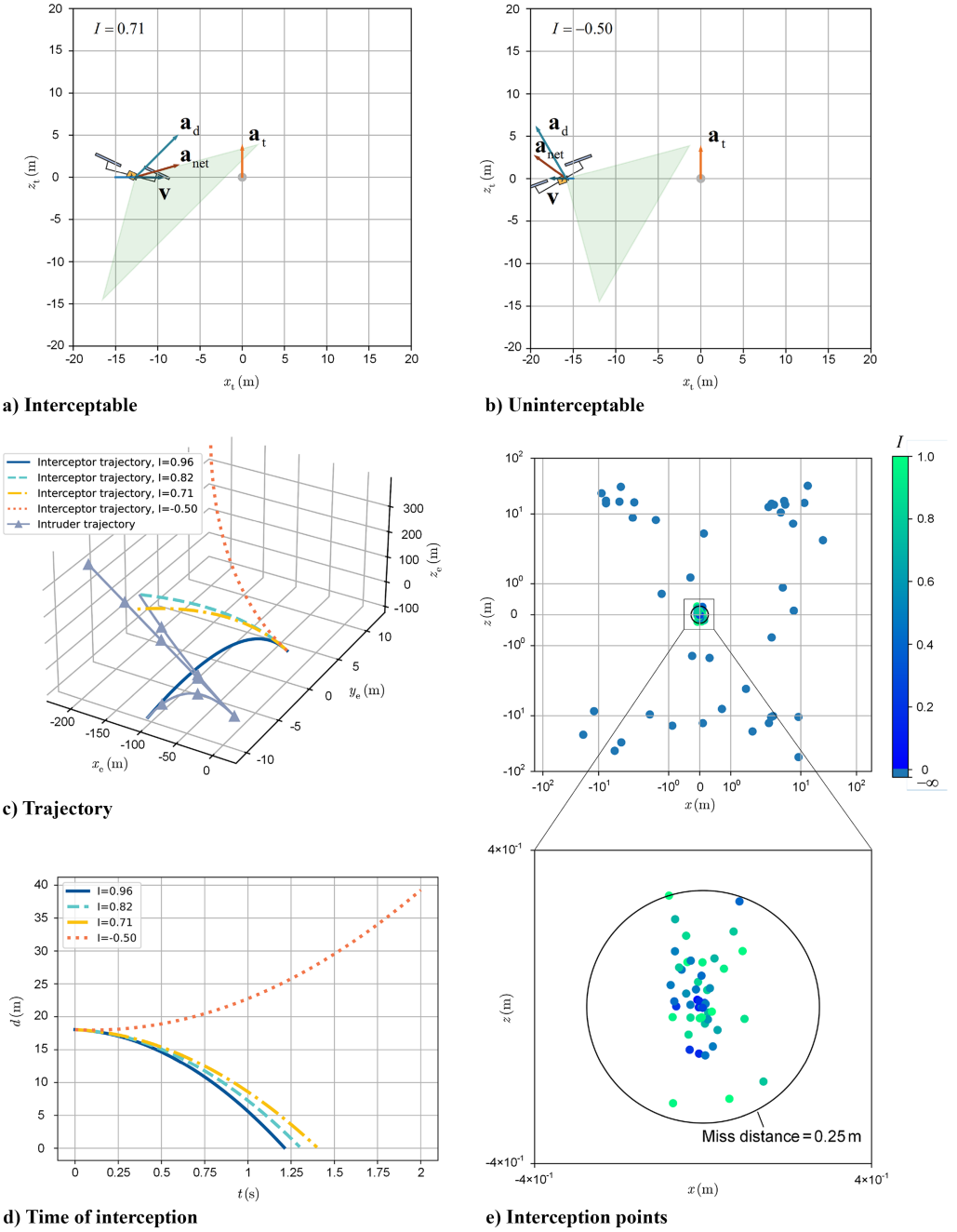


a) Optimal b) Spiral

c) Trajectory d) Time of interception

Fig. 5 Comparison of optimal strategy and spiral strategy.

Downloaded by BEIHANG UNIVERSITY on March 30, 2025 | http://arc.aiaa.org | DOI: 10.2514/1.G008527



a) Interceptable

b) Unterceptable

c) Trajectory

d) Time of interception

e) Interception points

Fig. 6 Interceptable and unterceptable situations of multicopters, and their statistical results.

$[0\ 0\ 0]^T$, and the velocity starts from rest; the initial state in TCS is shown in Eq. (11). The experiments specify four sets of parameters, as shown in Table 2. The interception trajectories are depicted in Fig. 6c, and the distance between the interceptor and the target varies with time, as shown in Fig. 6d. When $I = 0.96$, the target is intercepted at 1.21 s; when $I = 0.82$, the target is intercepted at 1.30 s; when $I = 0.71$, the target is intercepted at 1.40 s. Conversely, when $I = -0.5$, the interceptor fails to intercept the target at 2.00 s, with a relative distance of 39.25 m from the target. These results indicate that an interceptor with a larger DOI more effectively performs the interception task.

Table 2 Parameters of the interceptable and unterceptable cases

Case	$\tau_{\max}$	$\tau_{t,\max}$	α_{vfov}, deg	α'_{vfov}, deg	β, deg	δ_c, deg	I
Interceptable	2	0.5	120	90	30	−30	0.96
	2	1	120	90	30	0	0.82
	2	1	120	90	30	30	0.71
Unterceptable	2	1	90	60	0	60	−0.50

2. *DOI Determines Whether the Interceptor Can Complete the Interception Task*

The initial position of interceptors is set to $[0\ 0\ 0]^T$, while the initial positions of the targets are randomly generated within the range $[-30, -10] \times [-10, 10] \times [0, 20]$. The velocity magnitude is 10 m/s, and the direction is randomly generated. Each set of parameters is simulated 50 times, and the scatter diagram of the miss distance between the interceptor and the target within 100 s is obtained, as shown in Fig. 6e. We encapsulated all instances where $I > 0$ inside a circle centered at the origin, defining its radius as the experimental set miss distance, which specifically measures 0.25 m. It can be observed that the results for cases with $I > 0$ are all smaller than the physical size within 0.3 m. Additionally, the mean miss distance is 0.11 m, with a standard deviation of 0.09 m. In contrast, the results for cases with $I \leq 0$ are larger than the physical size. This

supports the validity of Theorem 1, affirming that $I > 0$ is a criterion for global LOS-constrained interceptability.

V. Multicopter Interception Flight Experiments

The efficacy and resilience of the proposed method have been thoroughly validated through extensive simulations, which provided a controlled environment to assess its performance. Building on the multicopter design recommendations and the insights gained from these simulations, real flight experiments were conducted to confirm the method's viability and applicability in real-world conditions.

A. Design of Flight Experiments

The multicopter designated as the interceptor in our real flight experiments is illustrated in Fig. 7. The interceptor multicopter is custom-designed, featuring an NVIDIA Jetson Xavier NX onboard computer and a front-facing CSI camera with a 120° HFOV and 90° VFOV. The camera was strapped down to the body, and seven sets of experiments were conducted with camera installation angles of 0°, ±15°, ±30°, and ±45°. The onboard computer performed target detection, target estimation, and high-speed intercept control algorithms [10].

As depicted in Fig. 7, the target intruder consisted of a red balloon tethered to a multicopter. The flight path of the target was predetermined to follow a rectangular pattern, which remained undisclosed to the interceptors. The precise location of the target was subject to variability due to both the movement of the multicopter carrying it and the influence of wind.

B. Flight Data Analysis

The data obtained from the aforementioned sets of experiments were subjected to interceptability analysis, the results of which are presented in Table 3. The experimental outcomes align well with the theoretical predictions. Among the interceptable experimental sets, the interceptor successfully intercepted the upper target in the fastest instance at an installation angle of 15°. For the experimental sets that were uninterceptable, the target repeatedly moved in and out of the edge of the FOV, and the interceptor ultimately failed to intercept the target. This failure was due to the camera installation angle being oriented too far downward, resulting in conflicting control commands to maintain the target within the FOV while keeping the interceptor close to the target. This can be observed in the nonsmooth trajectory. The experimental outcomes align with the hypotheses presented in this Note and serve to fulfill the research objective.

For additional experiments and detailed analysis, see the supplementary video: https://youtu.be/bz52TcHFS6A.

Table 3 Parameters of real flight experiments

Case	$\tau_{\max}$	$\tau_{t,\max}$	α_{vfov}, deg	α'_{vfov}, deg	β, deg	δ_c, deg	I
Interceptable	2	1	90	80	0	0	0.73
	2	1	90	80	0	−15	0.81
	2	1	90	80	0	−30	0.96
	2	1	90	80	0	−45	0.97
	2	1	90	80	0	15	0.69
Uninterceptable	2	1	90	80	0	30	−0.50
	2	1	90	80	0	45	$-\infty$

VI. Conclusions

This study delves into the interception capabilities of a specific class of interceptors within the LOS constraints. The salient conclusions are as follows:

1) The study introduces the definitions of global LOS-constrained interceptability and the DOI, affirming that an interception system is interceptable if the DOI is positive. Analytical criteria for the

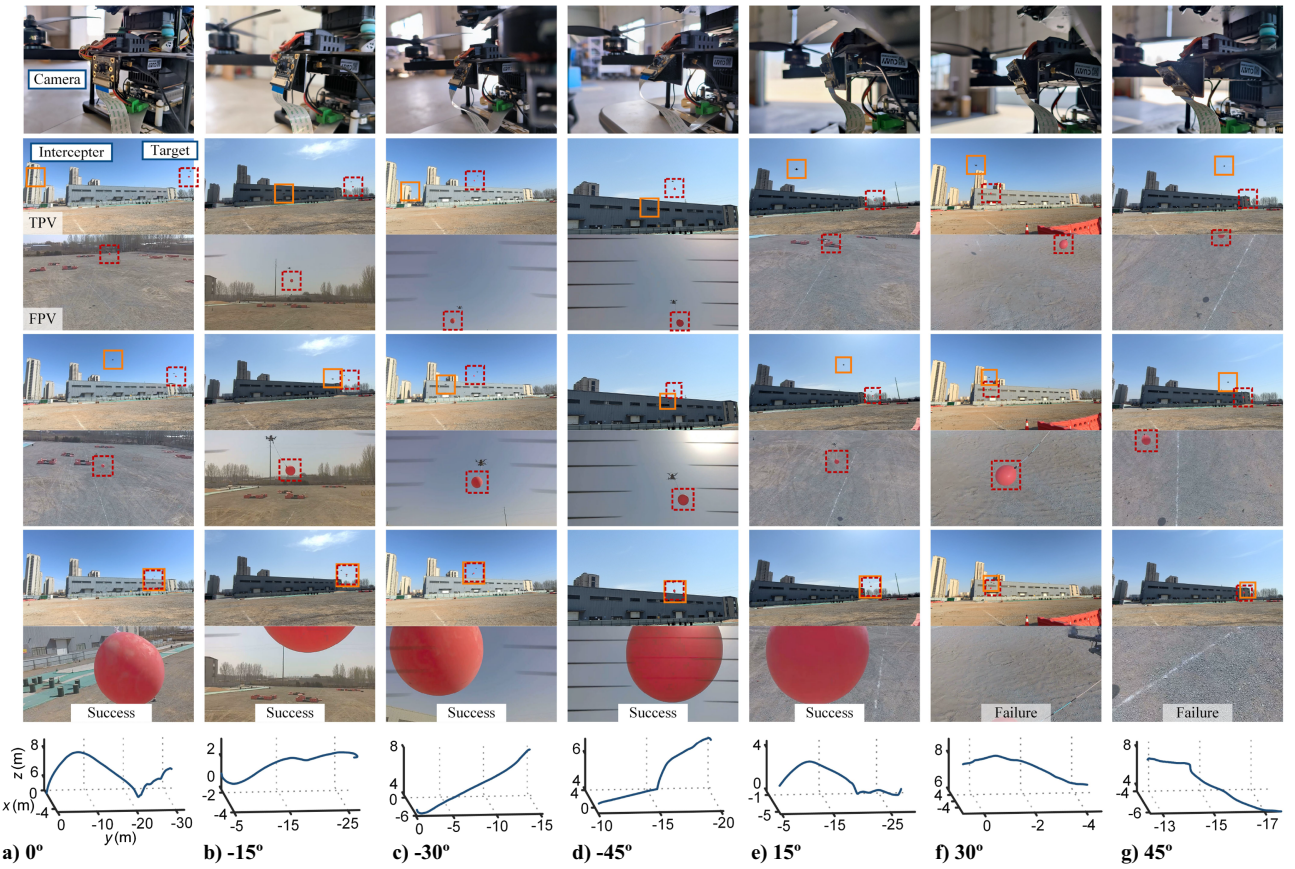


Fig. 7 Real flight experimental procedure with different camera installation angles. It includes third-person view (TPV) and first-person view (FPV). At the bottom is a plot of the interceptor's trajectory for each experiment.

Downloaded by BEIHANG UNIVERSITY on March 30, 2025 | http://arc.aiaa.org | DOI: 10.2514/1.G008527

DOI of multicopters have been established, accompanied by design recommendations.

2) Simulations reveal that interceptors with a DOI that positions the thrust direction nearer to the perception sensor's FOV center have superior interception capabilities. Additionally, a higher DOI facilitates the execution of interception tasks.

These findings are corroborated by real flight experiments, underscoring the DOI's practical relevance.

Future research will broaden these findings to encompass all interceptor types. Considering aerodynamics, such as those affecting fixed-wing aircraft and interceptor missiles, interceptability becomes a variable contingent on state conditions. Additionally, the concept of local interceptability warrants further exploration.

Appendix A: Detailed Derivation of the Interceptor's Flight Control Rigid Model in TCS

Starting from Eqs. (1) and (2) and using the definition of the TCS, we can express the relationship between the position vectors in the EFCS and TCS as

$$ {}^{e}\boldsymbol{p} - {}^{e}\boldsymbol{p}_t = \boldsymbol{R}_t^e \boldsymbol{p} \tag{A1} $$

Here, $\boldsymbol{R}_t^e$ is the rotation matrix from TCS to EFCS. The time derivative of $\boldsymbol{R}_t^e$ is given by

$$ \dot{\boldsymbol{R}}_t^e = \boldsymbol{R}_t^e [\omega_T]_\times \tag{A2} $$

where ω_T represents the angular velocity of TCS relative to EFCS. Differentiating Eq. (A1) with respect to time, we obtain

$$ {}^{e}\boldsymbol{v} - {}^{e}\boldsymbol{v}_t = \boldsymbol{R}_t^e [\omega_T]_\times \boldsymbol{p} + \boldsymbol{R}_t^e \dot{\boldsymbol{p}} \tag{A3} $$

This expression simplifies further to

$$ \boldsymbol{R}_t^{eT} ({}^{e}\boldsymbol{v} - {}^{e}\boldsymbol{v}_t) = \omega_T \times \boldsymbol{p} + \dot{\boldsymbol{p}} $$

Thus, we obtain the expression for $\dot{\boldsymbol{p}}$:

$$ \dot{\boldsymbol{p}} = \boldsymbol{R}_t^{eT} ({}^{e}\boldsymbol{v} - {}^{e}\boldsymbol{v}_t) - \omega_T \times \boldsymbol{p} \tag{A4} $$

Next, defining $\boldsymbol{v} \triangleq \dot{\boldsymbol{p}}$, we differentiate Eq. (A3) again:

$$ {}^{e}\dot{\boldsymbol{v}} - {}^{e}\dot{\boldsymbol{v}}_t = \boldsymbol{R}_t^e [\omega_T]_\times [\omega_T]_\times \boldsymbol{p} + \boldsymbol{R}_t^e [\dot{\omega}_T]_\times \boldsymbol{p} + \boldsymbol{R}_t^e [\omega_T]_\times \dot{\boldsymbol{p}} + \boldsymbol{R}_t^e [\omega_T]_\times \dot{\boldsymbol{p}} + \boldsymbol{R}_t^e \ddot{\boldsymbol{p}} $$

Simplifying this, we arrive at

$$ \boldsymbol{R}_t^{eT} \left(\frac{1}{m} {}^{e}\boldsymbol{f} - {}^{e}\boldsymbol{a}_t \right) = \omega_T \times (\omega_T \times \boldsymbol{p}) + \dot{\omega}_T \times \boldsymbol{p} + 2\omega_T \times \dot{\boldsymbol{p}} + \ddot{\boldsymbol{p}} $$

From this, the expression for $\ddot{\boldsymbol{p}}$ becomes

$$ \ddot{\boldsymbol{p}} = \frac{1}{m} \boldsymbol{f} - \boldsymbol{a}_t - \omega_T \times (\omega_T \times \boldsymbol{p}) - \dot{\omega}_T \times \boldsymbol{p} - 2\omega_T \times \dot{\boldsymbol{p}} $$

Here, the fictitious forces generated by the rotation of the TCS relative to the EFCS, including the Euler force, Coriolis force, and centrifugal force [30], are defined as

$$ \boldsymbol{f}_{\text{fic}} = m(-{}^{e}\dot{\omega}_T \times \boldsymbol{p} - 2\omega_T \times \boldsymbol{v} - \omega_T \times (\omega_T \times \boldsymbol{p})) $$

Thus, we obtain

$$ \dot{\boldsymbol{v}} = \frac{1}{m} \boldsymbol{f} - \boldsymbol{a}_t + \frac{1}{m} \boldsymbol{f}_{\text{fic}} \tag{A5} $$

By combining Eqs. (A2–A5), we obtain Eq. (3), which describes the interceptor's flight control rigid-body model in TCS.

Downloaded by BEIHANG UNIVERSITY on March 30, 2025 | http://arc.aiaa.org | DOI: 10.2514/1.G008527

Acknowledgments

This work was supported in part by the National Natural Science Foundation of China under (grant number 61973015) and in part by the Scientific Research Foundation of Beihang University.

References

[1] Panahi, F. H., Panahi, F. H., and Ohtsuki, T., "A Reinforcement Learning-Based Fire Warning and Suppression System Using Unmanned Aerial Vehicles," *IEEE Transactions on Instrumentation and Measurement*, Vol. 72, Dec. 2022, pp. 1–16. https://doi.org/10.1109/TIM.2022.3227558

[2] Miller, N., and Rogers, J., "Simultaneous Tracking of Multiple Ground Targets from a Multirotor Unmanned Aerial Vehicle," *Journal of Aerospace Information Systems*, Vol. 12, No. 3, 2015, pp. 345–364. https://doi.org/10.2514/1.I010345

[3] Dissanayaka, D., Wanasinghe, T. R., De Silva, O., Jayasiri, A., and Mann, G. K. I., "Review of Navigation Methods for UAV-Based Parcel Delivery," *IEEE Transactions on Automation Science and Engineering*, Vol. 21, No. 1, 2024, pp. 1068–1082. https://doi.org/10.1109/TASE.2022.3232025

[4] Floreano, D., and Wood, R. J., "Science, Technology and the Future of Small Autonomous Drones," *Nature*, Vol. 521, No. 7553, 2015, pp. 460–466. https://doi.org/10.1038/nature14542

[5] Ritchie, M., Fioranelli, F., and Borrion, H., "Micro UAV Crime Prevention: Can We Help Princess Leia?," *Crime Prevention in the 21st Century*, Springer, Berlin, 2017, pp. 359–376.

[6] Shi, X., Yang, C., Xie, W., Liang, C., Shi, Z., and Chen, J., "Anti-Drone System with Multiple Surveillance Technologies: Architecture, Implementation, and Challenges," *IEEE Communications Magazine*, Vol. 56, No. 4, 2018, pp. 68–74. https://doi.org/10.1109/MCOM.2018.1700430

[7] Zhu, X., "Analysis of Military Application of UAV Swarm Technology," *3rd International Conference on Unmanned Systems (ICUS)*, Inst. of Electrical and Electronics Engineers, New York, 2020, pp. 1200–1204. https://doi.org/10.1109/ICUS50048.2020

[8] Ghosh, S., Yakimenko, O. A., Davis, D. T., and Chung, T. H., "Unmanned Aerial Vehicle Guidance for an All-Aspect Approach to a Stationary Point," *Journal of Guidance, Control, and Dynamics*, Vol. 40, No. 11, 2017, pp. 2871–2888. https://doi.org/10.2514/1.G002614

[9] Yang, K., and Quan, Q., "An Autonomous Intercept Drone with Image-Based Visual Servo," *2020 IEEE International Conference on Robotics and Automation (ICRA)*, Inst. of Electrical and Electronics Engineers, New York, 2020, pp. 2230–2236. https://doi.org/10.1109/ICRA40945.2020.9197539

[10] Yang, K., Bai, C., She, Z., and Quan, Q., "High-Speed Interception Multicopter Control by Image-Based Visual Servoing," *IEEE Transactions on Control Systems Technology*, Vol. 1293, Sept. 2024, pp. 1–17. https://doi.org/10.1109/TCST.2024.3451293

[11] Stasinchuk, Y., Vrba, M., Petrlík, M., Báca, T., Spurný, V., Hert, D., Žaitlík, D., Nascimento, T., and Saska, M., "A Multi-UAV System for Detection and Elimination of Multiple Targets," *2021 IEEE International Conference on Robotics and Automation (ICRA)*, Inst. of Electrical and Electronics Engineers, New York, Vol. 2057, 2021, pp. 555–561. https://doi.org/10.1109/ICRA48506.2021.9562057

[12] Vrba, M., Stasinchuk, Y., Báca, T., Spurný, V., Petrlík, M., Hert, D., Žaitlík, D., and Saska, M., "Autonomous Capture of Agile Flying Objects Using UAVs: The MBZIRC. 2020 Challenge," *Robotics and Autonomous Systems*, Vol. 149, March 2022, Paper 103970. https://doi.org/10.1016/j.robot.2021.103970

[13] Tao, H., Lin, D., He, S., Song, T., and Jin, R., "Optimal Terminal-Velocity-Control Guidance for Intercepting Non-Cooperative Maneuvering Quadcopter," *Journal of Field Robotics*, Vol. 39, No. 4, 2022, pp. 457–472. https://doi.org/10.1002/rob.22059

[14] Li, J., Ning, Z., He, S., Lee, C.-H., and Zhao, S., "Three-Dimensional Bearing-Only Target Following via Observability-Enhanced Helical Guidance," *IEEE Transactions on Robotics*, Vol. 39, No. 2, 2023, pp. 1509–1526. https://doi.org/10.1109/TRO.2022.3218268

[15] Zhu, B., Zaini, A. H. B., and Xie, L., "Distributed Guidance for Interception by Using Multiple Rotary-Wing Unmanned Aerial

Vehicles," *IEEE Transactions on Industrial Electronics*, Vol. 64, No. 7, 2017, pp. 5648–5656.
https://doi.org/10.1109/TIE.2017.2677313

[16] Xie, H., Lynch, A. F., Low, K. H., and Mao, S., "Adaptive Output-Feedback Image-Based Visual Servoing for Quadrotor Unmanned Aerial Vehicles," *IEEE Transactions on Control Systems Technology*, Vol. 28, No. 3, 2020, pp. 1034–1041.
https://doi.org/10.1109/TCST.2019.2892034

[17] Wang, G., Qin, J., Liu, Q., Ma, Q., and Zhang, C., "Image-Based Visual Servoing of Quadrotors to Arbitrary Flight Targets," *IEEE Robotics and Automation Letters*, Vol. 8, No. 4, 2023, pp. 2022–2029.
https://doi.org/10.1109/LRA.2023.3245416

[18] Sultan, M. M., Biediger, D., Li, B., and Becker, A. T., "The Reachable Set of a Drone: Exploring the Position Isochrones for a Quadcopter," *2021 IEEE International Conference on Robotics and Automation (ICRA)*, Vol. 1715, Inst. of Electrical and Electronics Engineers, New York, 2021, pp. 7679–7685.
https://doi.org/10.1109/ICRA48506.2021.9561715

[19] Vinod, A. P., HomChaudhuri, B., Hintz, C., Parikh, A., Buerger, S. P., Oishi, M. M. K., Brunson, G., Ahmad, S., and Fierro, R., "Multiple Pursuer-Based Intercept via Forward Stochastic Reachability," *2018 Annual American Control Conference (ACC)*, IEEE, 2018, pp. 1559–1566.
https://doi.org/10.23919/ACC.2018.8431308

[20] Weintraub, I. E., Pachter, M., and Garcia, E., "An Introduction to Pursuit-Evasion Differential Games," *2020 American Control Conference (ACC)*, IEEE, 2020, pp. 1049–1066.
https://doi.org/10.23919/ACC45564.2020.9147205

[21] Hamandi, M., Usai, F., Sablé, Q., Staub, N., Tognon, M., and Franchi, A., "Design of Multirotor Aerial Vehicles: A Taxonomy Based on Input Allocation," *International Journal of Robotics Research*, Vol. 40, Nos. 8–9, 2021, pp. 1015–1044.
https://doi.org/10.1177/02783649211025998

[22] Du, G.-X., and Quan, Q., "Optimization of Multicopter Propulsion System Based on Degree of Controllability," *Journal of Aircraft*, Vol. 56, No. 5, 2019, pp. 2062–2069.
https://doi.org/10.2514/1.C035150

[23] Allenspach, M., Bodie, K., Brunner, M., Rinsoz, L., Taylor, Z., Kamel, M., Siegwart, R., and Nieto, J., "Design and Optimal Control of a Tiltrotor Micro-Aerial Vehicle for Efficient Omnidirectional Flight," *International Journal of Robotics Research*, Vol. 39, Nos. 10–11, 2020, pp. 1305–1325.
https://doi.org/10.1177/0278364920943654

[24] Yan, X., Kuang, M., Zhu, J., and Yuan, X., "Reachability-Based Cooperative Strategy for Intercepting a Highly Maneuvering Target Using Inferior Missiles," *Aerospace Science and Technology*, Vol. 106, Nov. 2020, Paper 106057.
https://doi.org/10.1016/j.ast.2020.106057

[25] Merkulov, G., Iceland, E., Michaeli, S., Riechkind, Y., Gal, O., Barel, A., and Shima, T., "Reinforcement Learning Based Decentralized Weapon-Target Assignment and Guidance," *AIAA SciTech Forum*, AIAA Paper 2024-0125, 2024.
https://doi.org/10.2514/6.2024-0125

[26] Bayoglu, T., and Akalin, G., "Reachability Analysis of an Aerodynamic Interceptor with Input Constraint," *AIAA SciTech 2022 Forum*, AIAA Paper 2022-2039, 2022.
https://doi.org/10.2514/6.2022-2039

[27] Jha, B., Bopardikar, S., Moll, A. V., and Casbeer, D., "Linear Quadratic Guidance Law for Joint Motion Planning of a Pursuer-Turret Assembly," 2024.
https://doi.org/10.48550/arXiv.2403.14997

[28] Kim, J., and Tahk, M.-J., "Co-Evolutionary Computation for Constrained Min-Max Problems and Its Applications for Pursuit-Evasion Games," *Proceedings of the 2001 Congress on Evolutionary Computation (IEEE Cat. No. 01TH8546)*, Inst. of Electrical and Electronics Engineers, New York, 2001, pp. 1205–1212.
https://doi.org/10.1109/CEC.2001.934328

[29] Quan, Q., *Introduction to Multicopter Design and Control*, Springer Singapore, Singapore, 2017, pp. 121–143.
https://doi.org/10.1007/978-981-10-3382-7_6

[30] Kibble, T. W. B., and Berkshire, F. H., *Classical Mechanics*, 5th ed., Imperial College Press, London, 2004.
https://doi.org/10.1142/p310

[31] Sanchez, A., Escareño, J., Garcia, O., and Lozano, R., "Autonomous Hovering of a Noncyclic Tiltrotor UAV: Modeling, Control and Implementation," *IFAC Proceedings*, Vol. 41, No. 2, 2008, pp. 803–808.
https://doi.org/10.3182/20080706-5-KR-1001.00138

[32] Corke, P. I., and Khatib, O., *Robotics, Vision and Control Fundamental Algorithms in MATLAB*, Vol. 73, Springer, Berlin, 2011.
https://doi.org/10.1007/978-3-642-20144-8

[33] Bertsekas, D., "Infinite Time Reachability of State-Space Regions by Using Feedback Control," *IEEE Transactions on Automatic Control*, Vol. 17, No. 5, 1972, pp. 604–613.
https://doi.org/10.1109/TAC.1972.1100085

[34] Brammer, R. F., "Controllability in Linear Autonomous Systems with Positive Controllers," *SIAM Journal on Control*, Vol. 10, No. 2, 1972, pp. 339–353.
https://doi.org/10.1137/0310026

[35] Ren, J., Dai, X., Quan, Q., Wei, Z.-B., and Cai, K.-Y., "Reliable Docking Control Scheme for Probe-Drogue Refueling," *Journal of Guidance, Control, and Dynamics*, Vol. 42, No. 11, 2019, pp. 2511–2520.
https://doi.org/10.2514/1.G003708

[36] Ohlmeyer, E. J., "Root-Mean-Square Miss Distance of Proportional Navigation Missile Against Sinusoidal Target," *Journal of Guidance, Control, and Dynamics*, Vol. 19, No. 3, 1996, pp. 563–568.
https://doi.org/10.2514/3.21658

M. Oppenheimer
Associate Editor

Downloaded by BEIHANG UNIVERSITY on March 30, 2025 | http://arc.aiaa.org | DOI: 10.2514/1.G008527